ASME Journal of Heat and Mass Transfer
Online journal at:
https://asmedigitalcollection.asme.org/heattransfer

Xiaohua Wu
School of Mechanical and
Automotive Engineering,
South China University of Technology,
Guangzhou 510641, China
e-mail: 651753474@qq.com

Longsheng Lu
School of Mechanical and
Automotive Engineering,
South China University of Technology,
Guangzhou 510641, China
e-mail: meluls@scut.edu.cn

Lanzhi Liang
School of Mechanical and
Automotive Engineering,
South China University of Technology,
Guangzhou 510641, China
e-mail: lyacelan@163.com

Xiaokang Mei
School of Mechanical and
Automotive Engineering,
South China University of Technology,
Guangzhou 510641, China
e-mail: meixk97@qq.com

Qinghua Liang
School of Mechanical and
Automotive Engineering,
South China University of Technology,
Guangzhou 510641, China
e-mail: 1622404890@qq.com

Yilin Zhong
School of Mechanical and
Automotive Engineering,
South China University of Technology,
Guangzhou 510641, China
e-mail: 2326563350@qq.com

Zeqiang Huang
Huizhou Desay SV Intelligent Transportation
Technological Institute Co., Ltd.,
Huizhou 516006, China
e-mail: Zeqiang.Huang@desaysv.com

Shu Yang
School of Mechanical and
Automotive Engineering,
South China University of Technology,
Guangzhou 510641, China
e-mail: yangshme@scut.edu.cn

Quick Prediction of Complex Temperature Fields Using Conditional Generative Adversarial Networks

Qualified thermal management is an important guarantee for the stable work of electronic devices. However, the increasingly complex cooling structure needs several hours or even longer to simulate, which hinders finding the optimal heat dissipation design in the limited space. Herein, an approach based on conditional generative adversarial network (cGAN) is reported to bridge complex geometry and physical field. The established end-to-end model not only predicted the maximum temperature with high precision but also captured real field details in the generated image. The impact of amount of training data on model prediction performance was discussed, and the performance of the models fine-tuned and trained from scratch was also compared in the case of less training data or using in new electronic devices. Furthermore, the high expansibility of geometrically encoded labels makes this method possible to be used in the heat dissipation analysis of more electronic devices. More importantly, this approach, compared to the grid-based simulation, accelerates the process by several orders of magnitude and saves a large amount of energy, which can vastly improve the efficiency of the thermal management design of electronic devices.

[DOI: 10.1115/1.4065911]

---

[1] Corresponding author.

Contributed by the Heat Transfer Division of ASME for publication in the Journal of Heat and Mass Transfer. Manuscript received September 16, 2023; final manuscript received July 2, 2024; published online July 20, 2024. Assoc. Editor: Antonio Jose Silva Neto.

Hengfei He
SZ DJI Technology Co., Ltd.,
Shenzhen 518057, China
e-mail: hehengfei@foxmail.com

Yingxi Xie[1]
School of Mechanical and Automotive Engineering,
South China University of Technology,
Guangzhou 510641, China
e-mail: xieyingxi@scut.edu.cn

1 Introduction

As the power of electronic devices grows, heat generation has become the primary reason for electronic failure [1,2], which makes thermal management increasingly significant. But the continuously increasing functionality and decreasing size of electronic devices make the thermal management more challenging [3,4]. For the thermal design of electronic devices, computer-aided engineering (CAE) simulation is most commonly used to address the challenges of coupled fluid dynamics and heat transfer [5–7]. But, when dealing with the complex CAE models, thousands of nodes are required to compute, which consumes a lot of time and energy [8], hindering the optimization of thermal design. To quickly calculate the temperature field distribution, researchers have tried different methods to reduce the computational workload.

The traditional CAE simulation transforms the continuous partial differential equations into algebraic equations at finite discrete points to iteratively calculate the steady-state temperature field by discretizing the calculation domain of flow and thermal field in space [9–11]. In previous work, in order to bypass long-time computation of partial differential equations, data-driven surrogate model [12–14] was established to fit the mapping of factors and results of experiments. Response surface approximations [15], Kriging method, artificial neural network [12], and other algorithms or integrated models [16] are used to regress the results of CAE simulation cases. Once the surrogate model is established, optimization algorithms such as evolutionary algorithms and genetic algorithms can obtain results like CAE at a rate of approximate instantaneous response, to find the optimal geometric structure in the design space. With the rapid development of machine learning, algorithms originally used in computer vision have made a certain contribution to the construction of surrogate models with higher fitting accuracy. Researchers have combined data from internal structural parameters with stress fields [17], flow fields [18], thermal fields [19], atomic potential energy [20], etc., and trained end-to-end models through supervised learning methods, which have shown great advantages in various fields.

Preliminary feasibility studies have been conducted by some researchers on heat source layout problems and heat dissipation structure design. Chen et al. [21] developed a feature pyramid network that was trained with more than 50,000 collected data to predict the temperature field of the volume-to-point heat conduction problem in a two-dimensional (2D) rectangular domain. Based on this surrogate model, discrete heat source layout was optimized by a neighborhood search-based layout optimization algorithm. Zhao et al. [22] also investigated the temperature field prediction problem for six typical cases of two-dimensional volume-to-point and volume-to-boundary heat source layout optimization, developed a fast feature pyramid network-based temperature field prediction model for heat source layout, and investigated the fine-tuning method between six cases. Chen et al. [23] introduced a conditional multi-attention generative adversarial network to produce realistic temperature solutions with high applicability in a bare sandy land scene with random distribution of signal stations. Kang et al. [24] employed two convolutional neural network (CNN) models as the generator and discriminator within a conditional generative adversarial network (cGAN) framework, respectively, to investigate the transient simulation results of mixed convection in horizontal channels with heated bottom surfaces. Edalatifar et al. [25] proposed a CNN model to study the heat transfer processes under various two-dimensional geometric boundary conditions, incorporating the mean maximum mean squared error as the loss function. Yang et al. [18] proposed a surrogate model for temperature distribution and pressure distribution based on Pix2pix model and combined it with genetic algorithm to optimize the shape of needle fins. Advanced and comprehensive thermal simulations are key to achieve optimal thermal designs in electronic devices. However, current surrogate models that allow for rapid prediction of thermal simulations are not ideal for real-world scenarios. This creates challenges such as difficult data acquisition, the requirement for substantial amount of training data.

Herein, a general and highly extensibility approach was proposed to encode geometry and bridge the structure design and temperature field. Specifically, cGAN method was used to establish a mapping model with a high reduction of ground truth details. First, the temperature contour collected in the natural convection cases was used to train different models. The output was then compared with test set for contour details, overall accuracy, and image clarity. Second, training sets with varying sizes were used to train the same model, and the accuracy of the trained models was compared. Third, the air-cooling cases data were collected and used for model transfer learning which was superior to training the model from scratch. In addition, energy and time consumption measurements were also carried out. Compared to the CAE method, the proposed approach can speed up the process by several orders of magnitude and save a lot of energy, which helps optimize thermal design.

2 Material and Methods

2.1 Computer-Aided Engineering Calculation. The scenario studied here is from a common in-vehicle domain controller, and its complex structure has been simplified to shorten the time required. In response to the extensive temperature requirements for testing environments within the automotive industry, this domain controller is placed in an 85 °C environment with ten chips of variable size and power built in. Only three main components, the top cover, printed circuit board (PCB), and bottom cover, are considered. The contour image data were derived from the ICEPAK software. Key variables such as chip, bump, and fin geometry parameters were parametrically modeled in natural convection cooling and air-cooling heat dissipation projects. Stopping criterion of the set iteration was that the residual flow and energy fell below 10^{-3} and 10^{-7}, respectively, or the number of iterations had reached 100 steps. The required temperature contour of the PCB top surface was saved in a folder location by the ICEPAK program after iterations. To facilitate the subsequent program to convert the temperature value from the pixel value, the generated contour was limited to a fixed temperature range (from 85 °C to 150 °C) to avoid exceeding the maximum temperature limit which would preclude complete display, and the linear mapping method was used to map between the color and temperature.

The simulation model was established using ICEPAK built-in modules including PCB, block, sources, enclosure, and heatsink. Initially, a cabinet was defined as the simulation domain, which was characterized by six opening walls and measured $300 \times 160 \times 450\,\mathrm{mm}^3$. A PCB, with dimensions of $200 \times 1.6 \times 300\,\mathrm{mm}^3$ and consisting of 19 interleaved layers of FR-4 and Cu, was then constructed. The in-plane and normal effective thermal conductivities was automatically calculated to be 1.75 W/(m K) and 0.44 W/(m K), respectively. As shown in Fig. S1 available in the Supplemental Materials on the ASME Digital Collection, two 1 mm thick solid blocks and a 0.0026 mm thick source were utilized to emulate the actual chip. Above the chip, a plate was placed to simulate thermal interface material (TIM) with a thermal conductivity of 6 W/(m K) and an equivalent thickness of 1 mm. ICEPAK automatically computed the contact thermal resistance for each TIM based on its surface area. Additionally, an enclosure was designed to represent the in-vehicle domain controller's cavity and outer shell, measuring $200 \times 27.1 \times 300\,\mathrm{mm}^3$, with each face made from 2 mm thick extruded aluminum. The heatsink was detailedly modeled within the ICEPAK, facilitating control over parameters such as fin thickness, number, and height. The schematic diagram of the built ICEPAK model is shown in Fig. S2 available in the Supplemental Materials. This configuration supported the development of parametric models using ICEPAK's inherent modeling capabilities. This approach overlooked features such as mounting holes and signal line exits, inevitably leading to discrepancies between the parametric model and the actual controller.

Because the fin type did not participate in the parameterization process, the models of rectangular fin and cross fin in the natural convection cooling were built, respectively. To ensure that each parameterization case remains stable in the iterative process and accurate enough, the mesh independence of parameterization was studied. By increasing the number of grid divisions in the X, Y, and Z directions (Fig. S3 available in the Supplemental Materials) of fins, the iterative results were more accurate. The combination of parameters that began to fluctuate at the maximum PCB temperature was selected (Table S1 available in the Supplemental Materials). The mesh number of fins in X, Y, and Z directions was 6, to ensure the independent of mesh. In the following part, the data verified by convergence and mesh independence principle were regarded as ground truth. The meshing and solution conditions in different cases were consistent through optimization module of ICEPAK.

To ensure the accuracy of the PCB steady-state temperature field obtained from the parametric model, the temperature of ten chips in an in-vehicle domain controller were measured and compared with the simulation results. The comparison of the geometrical structure and the difference in some parameters between the actual in-vehicle domain controller and the parametric simulation model is shown in Fig. S4 and Table S2 available in the Supplemental Materials, respectively. The comparison of chip thickness settings with the parametric model is shown in Table S3 available in the Supplemental Materials. The chip layout and fin arrangement of the in-vehicle domain controller are shown in Fig. S5 available in the Supplemental Materials. We used ceramic heating pads to replace the actual chips for heat generation, and thermocouple wires were installed on each chip for temperature measurement (Fig. S6 available in the Supplemental Materials). A TIM with a thermal conductivity of 6 W/(m K) was used between the chips and the bumps to ensure effective heat transfer. We put the in-vehicle domain controller mounted in a climate chamber using a thermocouple to measure the temperature of the chip. The ambient temperature was set to 85 °C.

2.2 Development and Training of Models.

The deep learning (DL) models were implemented using PYTORCH [26], which is a general framework in PYTHON. Spatially adaptive pixelwise network (ASAP-net) [27], a state-of-the-art (SOTA) model in the domain of image generation, operates on each pixel through a multilayer perceptron (MLP) to predict every pixel of the generated image. ASAP-net employs a CNN to predict the weights of the MLP, thereby circumventing the need to manipulate a lot of parameters during training. This approach significantly accelerates the training process while preserving the capability to reproduce rich details and contours. Consequently, it has been selected as the predictive model for temperature fields in this study. In the domain of image generation, Pix2pix [28] is recognized as one of the early and classical work, utilizing a U-net [29] architecture as the backbone network for its generator. These methodologies exemplify the typical performance of generative and supervised approaches in this task. Consequently, Pix2pix and U-net models have been established as baseline models for comparison of performance. These models were developed and trained, respectively, according to the structure at their publications. ASAP-net is a typical cGAN, comprised of a generator and a discriminator. The generator is divided into two components: a CNN operating at low-resolution process and a MLP for high-resolution process, with the specific architectures detailed in Tables S4 and S5 available in the Supplemental Materials, respectively. The discriminator consists of multiple layers of CNN, as shown in Table S6 available in the Supplemental Materials. The inputs and outputs of the ASAP-net were three-channel images, which were resized to a resolution of 256×256 pixels prior to training. All the models and datasets can be found at this link.[2]

In the training of CNN, the Adam optimizer is widely utilized by scholars for its ability to rapidly approach an approximate optimal solution with training stability and minimal manual parameter adjustments. Thus, the Adam optimizer, with hyperparameters $\beta1$ set to 0.5, $\beta2$ set to 0.999, and learning rate set as 2×10^{-4}, was utilized to solve the trainable parameters in three models. The batch size of each training step was 1. All models were trained 500 epochs equally at a computer with GeForce RTX 3090.

When comparing the impact of the amount of training data on model performance, 2, 4, 8, 16, 32, 64, and 128 cases were randomly selected from natural convection dataset by random sampling, respectively. Another 50 data were randomly selected as the test set to verify trained models. To reduce the influence of noise by data composition, the above experiments were repeated 20 times.

When evaluating the performance of the fine-tuning model, 66 air-cooling cases were randomly divided into training set (16 cases) and test set (50 cases), and then used for training with random weights and pretrained weights from natural convection dataset, respectively. Similarly, to maintain the generality of the conclusion, this process was repeated 20 times.

2.3 Surrogate Model Evaluation.

To quantitatively compare the performance differences of the models, the comparison between model output images and the ground truth was studied. Both were linearly mapped to the real temperature value. After obtaining two temperature matrices, the maximum temperature relative error (MTRE) and the mean heatmap relative error (MHRE) were calculated as follows:

$$\mathrm{MTRE} = \left| \frac{T_{\mathrm{DL}} - T_{\mathrm{CAE}}}{T_{\mathrm{CAE}} - 273.15} \right| \times 100\% \tag{1}$$

$$\mathrm{MHRE} = \frac{\sum_{i}^{n} \sum_{j}^{m} \left| \frac{\mathrm{DL}_{ij} - \mathrm{CAE}_{ij}}{\mathrm{CAE}_{ij} - 273.15} \right|}{n \times m} \times 100\% \tag{2}$$

where T_{DL} was the maximum temperature of DL predictions, and T_{CAE} was the maximum temperature of CAE simulation results in Eq. (1). In Eq. (2), DL_{ij} and CAE_{ij} represented the temperature at

---

[2] https://gitee.com/wuxh_65175/CFD-cGAN

positions (i, j) of the results of machine learning prediction and CAE simulation, respectively.

Structural similarity metric (SSIM) has been widely used in image processing and computer vision to evaluate image similarity. Here, SSIM was introduced for evaluating the similarity between predicted and actual temperature field image. SSIM evaluates the restoration effect by comparing the structure, luminance, and contrast between two images, which is calculated by the following equation [30]:

$$\mathrm{SSIM}(x, y) = \frac{(2\mu_x\mu_y + C_1)(2\sigma_{xy} + C_2)}{(\mu_x^2 + \mu_y^2 + C_1)(\mu_x^2 + \mu_y^2 + C_2)} \tag{3}$$

where μ_x, μ_y was the mean of the two temperature field images x, y, σ_{xy} was the covariance of the two images x, y, and C_1 and C_2 represent constants. All subsequent calculations of SSIM were performed using the skimage library.

2.4 Dataset Preparation. Each parametric model, including rectangular natural convection cooling, cross fin natural convection cooling, and rectangular air cooling, generated some steady-state temperature field images through random parameter groups.

Paired data (Fig. 1) used in cGAN training consisted of a ground truth and a geometry label. According to the parameter group values corresponding to this case, the fin height, bump height, and chip power in geometry were mapped, respectively, to the red, green, and blue channels to generate the geometry label. Specifically, the mapping method is shown as follows:

$$(R, G, B) = 255 - \left(5 \times H_{\mathrm{sink}}, 5 \times H_{\mathrm{bump}}, 32 \times \frac{P_{\mathrm{chips}}}{0.01 \times w \times h}\right) \tag{4}$$

where H_{sink} (mm), H_{bump} (mm), and P_{chips} (W) were the height of the fin, the height of the bump, and the thermal power of chips. The w (mm) and h (mm) in the equation were the 2D geometric size of the chips. To ensure the absence of overlap among randomly generated chips and to address potential deficiencies in the dataset regarding temperature mapping in specific areas, the Latin hypercube sampling [31] method was employed for determining chips initial positions. Upon generation, the initial layouts of these chips were systematically inspected. In cases where overlap is detected, the positions of the overlapping chips would be randomly resampled until each chip was confirmed to be nonoverlapping.

2.5 Time and Energy Consumption. When executing CAE programs and ASAP-net models, the computer mainly used the computing resources of central processing unit (CPU) and graphics processing unit (GPU), so the energy and time consumption of CPU and GPU under a certain time were measured. Due to the time consumed by different programs of CAE varies greatly, two programs were selected from nature convection cooling and air-cooling heat dissipation scenarios for the power tests, respectively. In the training process of ASAP-net, several training scripts with different training set sizes were selected. The testing process of ASAP-net was to test the power consumption of predicting 1000 cases. In addition, the precise time required to predict a temperature field without reading data and preparing the model was also measured.

To ensure the fairness of the comparison, all measurements were carried out on the same workstation (Dell Inc, Round Rock, TX), which had ten Intel cores and an NVIDIA GeForce RTX 3090 (Nvidia Corporation, Santa Clara, CA). The power consumption monitoring of CPU was completed by the software power gadget 3.6 provided by Intel. The power consumption of GPU was monitored through NVIDIA's system management interface. To eliminate the influence of computer standby power consumption, the computer power consumption was measured many times without executing any programs. The influence of no-load power consumption was subtracted before calculating any power. The detailed power curve and measurement results are shown in Fig. S7 available in the Supplemental Materials on the ASME Digital Collection.

3 Results

3.1 Heat Dissipation Scenario Definition. In this paper, the influences of heat sink structure and chips layout on PCB temperature field were studied. As shown in Fig. 1, the temperature field of an electronic device under natural convection was discussed. Several chips with fixed heating power were placed inside the electronic device. The heat emitted was transferred to the heat sink through the heat conduction bumps, and the whole heat was removed through the air convection. After the geometry information in the electronic device were collected and encoded into a simple image, it formed a paired data with the ground truth calculated by the CAE.

Geometric parameters, including chip layout, bump layout, and fin shape, are encoded into the three-color channels of an image. The chip's size and positional distribution significantly influence the distribution and contour of the temperature cloud map. The fins, key in dissipating heat, affect the overall temperature magnitude. The bump serves as a crucial component for conducting heat to the fins, and its contact area with the TIM notably impacts the chip's final temperature. As shown in Fig. S8 and Table S7 available in the Supplemental Materials, an increase in the bump's contact area decreased the maximum temperature of the chip and slightly raised the temperatures of other chips, due to the limited heat dissipation capacity of the fins. In contrast, the absence of contact area led to a sharp increase in chip temperature (Fig. S9 available in the Supplemental Materials). The observed differences between the outcomes of stagger bump and without the bump can be attributed to airflows induced by the chip's heat near the protrusion (Fig. S10 available in the Supplemental Materials). Consequently, the bump is as critical a design parameter as the chip layout and fin parameters.

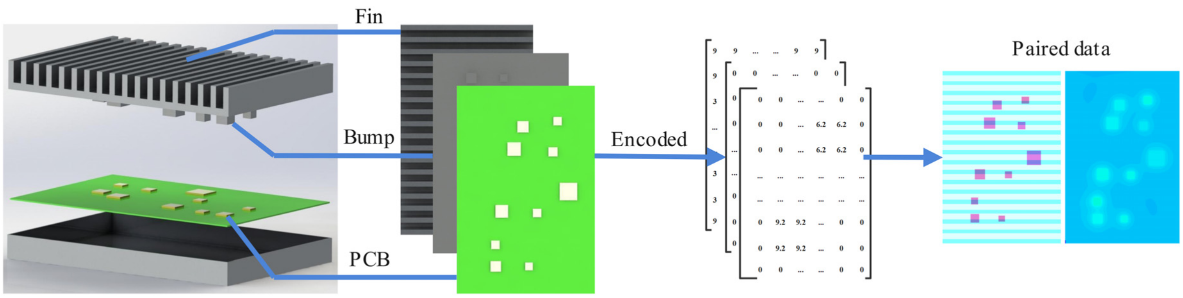

Fig. 1 The fin distribution, heat dissipation bump distribution, and chips layout on the thermal model of electronic device were simply encoded into three-channel values of a color image. The temperature contour screenshot calculated by CAE was cut by digital image processing technology to obtain the ground truth. Ground truth and geometry coded images formed a matching dataset for DL models training.

In established ICEPAK model, the Boussinesq approximation was utilized to solve governing equations of natural convection. The Boussinesq approximation posits that, within the governing equations of natural convection, the density term in the buoyancy component of the momentum equation ρg is a linear function of temperature

$$\rho_\infty - \rho \approx \rho\beta(T - T_\infty) \tag{5}$$

where ρ_∞ represents the ambient air density, T_∞ denotes the ambient air temperature, and β is the coefficient of thermal expansion of the surrounding air. Following the establishment of the model, the Rayleigh number was estimated by ICEPAK to be $1.8878 \times 10^7 < 10^9$, and the Prandtl number to be 0.7085. Consequently, a laminar flow model was selected for subsequent computations.

In simulations involving dense fin arrays, the discrete ordinates model is commonly employed due to its lower memory requirements. Consequently, the discrete ordinates model was selected to solve the radiative heat transfer for the established model.

Although the model is put in an open space, the heat sources must anticipate the heat through conduction via thermal conductive pads, bumps, and heat sinks. Therefore, equations that govern the conduction phenomenon are also considered

$$\frac{\partial}{\partial t}(\rho h) = \nabla \cdot (k\nabla T) \tag{6}$$

And in the fluid region the equation would be

$$\frac{\partial}{\partial t}(\rho h) + \nabla \cdot (\rho h \mathbf{v}) = \nabla \cdot (k\nabla T) \tag{7}$$

where ρ is density, k is the molecular conductivity, h is the enthalpy, and S_h is the source term.

Within the in-vehicle domain controller, when heat flux was transferred to the inner wall, it was necessary to consider the contributions from both the PCB and the air. The governing equation is expressed as follows:

$$-k_w\left(\frac{\partial T}{\partial n}\right)_w = -k_a\left(\frac{\partial T}{\partial n}\right)_a - k_p\left(\frac{\partial T}{\partial n}\right)_p \tag{8}$$

Here, $k_w(\partial T/\partial n)_w$ denotes the heat flux from the solid wall surface to the exterior, $k_a(\partial T/\partial n)_a$ indicates the heat flux from the fluid to the inner wall surface, and $k_p(\partial T/\partial n)_p$ represents the heat flux from the PCB to the inner wall surface.

When heat was transmitted from the outer wall to the air, the primary mechanism involved was convective heat exchange at the solid surface. The governing equation is expressed as follows:

$$-k_w\left(\frac{\partial T}{\partial n}\right)_w = h_w(T_w - T_a) \tag{9}$$

Here, h_w represents the convective heat transfer coefficient, T_w is the temperature at the outer wall surface, and T_a is the ambient temperature of the fluid. During the solution process, the boundary conditions employed entailed an ambient temperature of 85 °C, with adiabatic conditions at the boundaries of the cabinet.

Common cooling technologies, including natural convection cooling and air cooling, were studied in this paper. The datasets of natural convection cooling were collected and used to evaluate the performance of different DL methods and the impact of different training set scale on model performance. Due to the large gap in cooling capacity, the dataset of air cooling was used to verify the migration ability of models. When the trained model processed inconsistent data, the model could not reproduce the mapping of the pretrained data well. However, the trained surrogate model can be migrated to a new distribution by fine-tuning the weights. The natural convection dataset included 220 cases in total, which was randomly split into the training set (170 cases) and test set (50 cases). The air-cooling dataset included 66 cases in total, of which only 16 cases were used for fine-tuning, and the remaining 50 cases were used to verify the performance of the migrated model.

In order to verify the accuracy of the data obtained from the established parametric simulation model, we used a certain model of an in-vehicle domain controller (Fig. 2) for experimental verification. Since the PCB dimensions of this in-vehicle domain controller were not consistent with the parametric model, we used one of the boundaries as a reference to build a parametric model with consistent distribution and relative distance of each chip for comparison. In the empirical testing, the external dimensions of the in-vehicle domain controller were kept consistency with the parametric model ($200 \times 300\,\mathrm{mm}^2$). However, taking into consideration the space required for actual installation and cable accommodation, a physically smaller PCB than that specified in the parametric model was utilized. To minimize the potential impact of this deviation on the experimental outcomes, the layout and power of the chips were maintained uniformly (Table 1). The conversion layout method is shown in Fig. S4(*a*) available in the Supplemental Materials on the ASME Digital Collection. The selected domain controller heat sink was pin-fin, the specific chip parameters are shown in Table 2, and the specific calculation method with the fin layout is shown in Fig. S4(*b*) available in the Supplemental Materials.

The in-vehicle domain controller was placed in an 85 °C environment and supplied with the corresponding electrical energy to run at full power. The temperature rise profile obtained for each chip is shown in Fig. 3. Meanwhile, to verify the accuracy of the parametric model output temperature field, a detailed model that was consistent with each parameter of the in-vehicle domain controller was constructed. The temperature comparison of each chip for the measured, detailed, and parametric models is shown in Table 3. It can be found that the temperature error of each chip in the parametric model was less than 10 K. There were many parameter differences that would lead to errors, especially the effects of PCB size, thermal

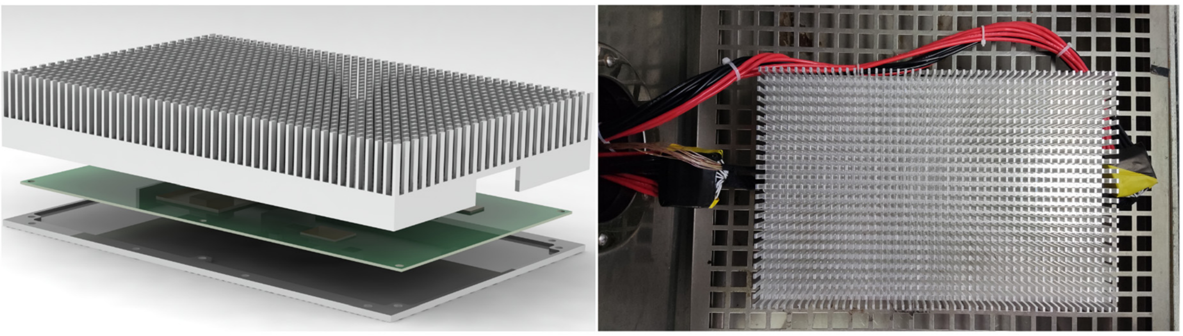
(*a*) (*b*)

Fig. 2 In-vehicle domain controller used to validate the accuracy of the parametric simulation model: (*a*) detailed model of the in-vehicle domain controller and (*b*) actual experimental diagram of the in-vehicle domain controller

Table 1 Chip layout of in-vehicle domain controller

Chip ID	Chip_w (mm)	Chip_l (mm)	Chip_x (mm)	Chip_z (mm)	Chip_q (W)	Chip_t (mm)
1	50	50	92	100	21.24	2
2	25	20	208	135	5.12	1.3
3	10	10	185	76	7.83	1.3
4	15	25	60	84	7.85	1.3
5	20	15	232	32	2.53	1.3
6	25	25	93	25	2.99	1.3
7	7	5	128	80	2.54	1.3
8	15	28	40	32	3.96	1.3
9	20	10	125	56	4.98	1.3
10	10	25	160	86	1.60	1.3

Table 2 Pin-fin size parameters for in-vehicle domain controller

Fin properties	Tim_t (mm)	Tim_k (W/(m K))	Fin_h (mm)	Fin_l1 (mm)	Fin_n1	Fin_l2 (mm)	Fin_n2
Value	0.5	6	28	2	50	4	25

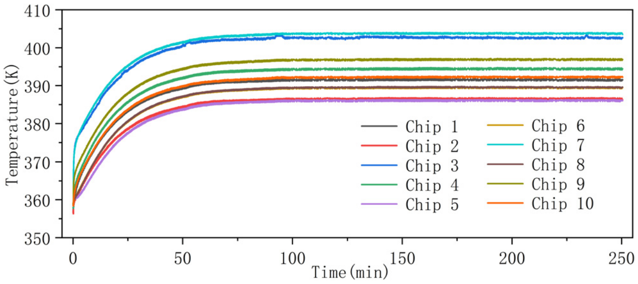

Fig. 3 Temperature trends of the in-vehicle domain controller operating at full power in an 85 °C environment

grease, casing material, and chip thickness. In contrast, the temperature errors of the established detailed models were all below 3 K, indicating that the PCB temperature field distribution of the detailed model was sufficiently similar to the actual temperature field. As shown in Fig. 4, the temperature field output of the detailed model and the parametric model were used for comparison. The contours and temperature distributions were sufficiently similar (Table 4).

3.2 Conditional Generative Adversarial Networks Development. The DL method implemented in this study was ASAP-net which is a SOTA algorithm of cGAN. The model consists of generator and discriminator for confrontation training (Fig. 5). In our work, the generator was used to receive the geometry label and generate the corresponding temperature field.

In contrast to the SOTA temperature prediction models that employ filters with shared parameters, the MLPs within ASAP-net are executed on pixelwise weights, with unique parameters for each pixel. This ensures the model's robust image representation capabilities. Moreover, the parameters of each MLP are not obtained via gradient descent optimization; instead, they are predicted from low-resolution input images using a CNN. This approach not only enhances the computational speed of the model but also circumvents the need for extensive model parameters. The MLP weights were filled with the output using a nearest neighbor interpolation upsampling.

The discriminator was used to distinguish the ground truth from the fake field generated by the generator. To increase the receptive field of the image without using a larger and deeper patch network, a multiscale patchGAN network was implemented to classify real and fake images. Image of different sizes was cut out with different numbers of patches which were sent to a five-layer CNN binary classifier.

After epochs of training against each other, the two components eventually reached the Nash equilibrium [32]. Once the cGAN model is trained, the generated temperature field would be so close to the ground truth that the discriminator could not separate the pictures. To figure out the advantages of cGAN over CNN methods, Pix2pix [28], U-net [29], and ASAP-net [30] were implemented to compare the performance. The Pix2pix loss function is defined as

$$\text{loss}_{\text{Pix2pix}} = \mathcal{L}_{\text{cGAN}}(G, D) + \lambda \mathcal{L}_1(G) \tag{10}$$

In our implementation, $\mathcal{L}_{\text{cGAN}}(G, D)$ was taken as the loss function of the mean square error between the classification of the discriminator in the generator and the actual category. $\mathcal{L}_1(G)$, an L1 loss, was a function used to measure the difference between the generated image and the ground truth. λ was a super parameter used to weigh the relative importance of two errors, which was set to a constant value of 100 in practice.

Table 3 Comparison of the temperature of each chip for the measured, detailed, and parametric models

Chip ID	Actual temperature (K)	Detail model (K)	$\Delta T1$ (K)	Parametric model (K)	$\Delta T2$ (K)
1	391.5	393.65	−2.15	386.41	5.08
2	386.25	387.35	−1.1	380.06	6.18
3	402.65	402.75	−0.1	401.65	0.99
4	394.45	394.05	0.4	387.88	6.56
5	386.1	385.05	1.05	377.17	8.92
6	389.45	388.55	0.9	381.07	8.37
7	403.55	402.85	0.7	401.14	2.41
8	389.6	388.05	1.55	381.01	8.58
9	396.9	394.65	2.25	388.75	8.14
10	392.25	391.85	0.4	383.80	8.44

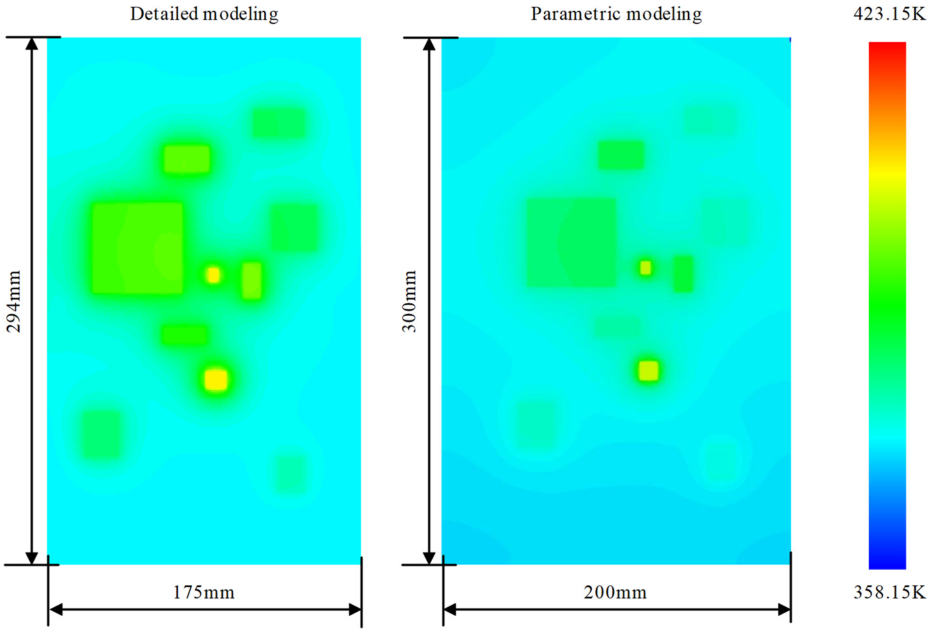

Fig. 4 Temperature field comparison of detailed and parametric model that were consistent with the parameters of the in-vehicle domain controller

Table 4 Comparison of time and electric energy consumed in executing different programs

Programs	Time (s/case)	Energy (mWh/case)
Natural convection	1652.00	36,952.9
Air cooling	3144.00	73,085.6
ASAP-net training	0.0645387	6.63687
ASAP-net test	0.0453333	2.14443

The U-net loss function is defined as

$$\mathrm{loss}_{\mathrm{U-net}} = \mathcal{L}_1(G) \tag{11}$$

Different from the loss function of Pix2pix, only the difference between the generated image and the ground truth was used as the optimization direction of the generator.

3.3 Performance Comparison of Models. Temperature field information is crucial for predictable optimization methods, which can obtain temperature values and gradients in each direction to support optimization. And a number-to-number surrogate model [33,34] to achieve temperature prediction at every point of the temperature field is not worth the effort. This shows that the important feature of 2D model compared with number-to-number model is accurate field prediction. The comparison between the predicted results and the ground truth is shown in Fig. 6.

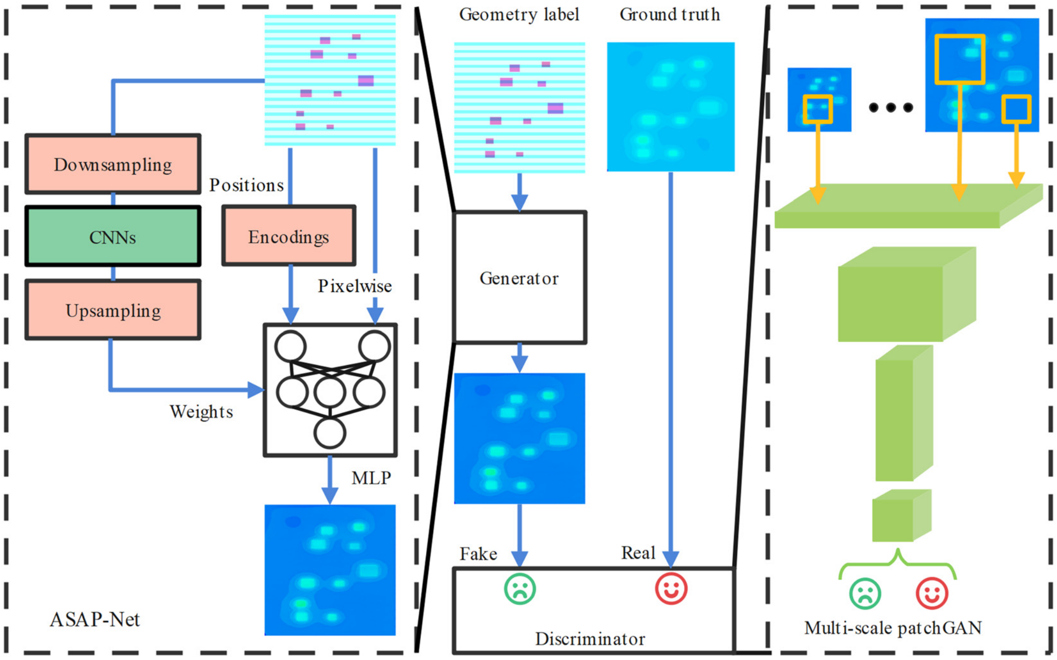

Fig. 5 The synthesized temperature field could be obtained by inputting the geometry label into the generator, and the discriminator classified the synthesized image and ground truth

Pix2pix, with U-net as its generator architecture, was one of the earliest image translation model using cGAN method. In our implementation, U-net only used L1 loss function to optimize the model, while Pix2pix combined the loss from discriminator to train generator. Therefore, the output of Pix2pix had more clear contours and image details instead of blurred regions (Fig. 6). It suggested that after the adversarial training against the generator, the discriminator learned to judge the reality of the image by distinguishing the contour distribution around the chips. Under the supervision of the discriminator, the generator was equipped with the ability to map fine contours and the heat transfer characteristic which was critical to engineering analysis.

From the temperature field and output characteristics of each model, the PCB temperature field generated by this electronic device in a harsh thermal environment is more strongly influenced by the chip layout than the fin layout. This is an advantage for the two models structured as U-net, which can be found to easily reproduce the temperature trend around the fins, but do not have the ability to obtain a clear and realistic contour profile like ASAP-net. This is because ASAP-net skillfully combines the two information streams of full-resolution and low-resolution to obtain the global information while maintaining the integrity of local high-frequency signal. As shown in Fig. 7, ASAP-net output was generally closer to ground truth temperature values, with finer contours in some details. The high-temperature region of ASAP-net results had a contour closer to ground truth than the remaining two models. In the low-temperature region, there were still contours that did not correspond to the ground truth. We also find ASAP-net to have higher SSIM values than two models. This indicated that the temperature distribution generated by ASAP-net was closer to the actual values. The absolute error values of the outputs of the three models with respect to ground truth were also used for comparison as shown in Fig. 7. Pix2pix had a larger output than U-net, probably because Pix2pix tended to generate more realistic contours, while U-net tended to generate temperature values consistent with the real temperature field. Even though ASAP-net still had many errors in generating some local contours, the errors were much lower than those in the other two models.

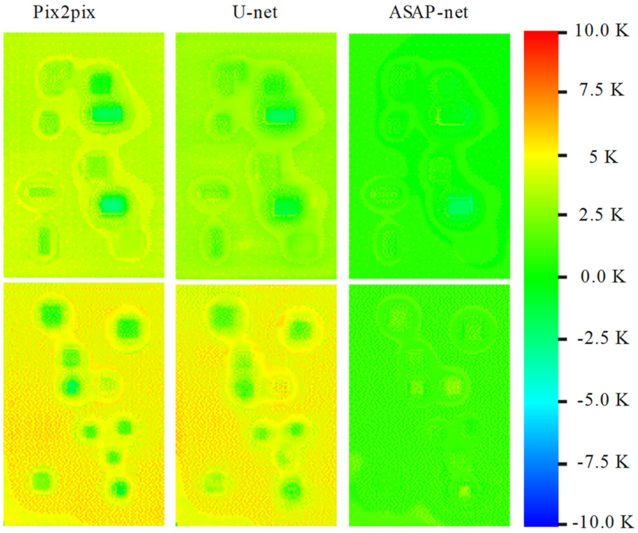

Fig. 7 Comparison of absolute value errors in the prediction results of different models

Therefore, ASAP-net is considered to be a better surrogate method for the mapping from geometry to temperature field in the electronic device. Compare the maximum temperature from ASAP-net prediction and ground truth (Fig. 8), it can be found that the prediction error of most examples is almost lower than 5 K. To evaluate the difference further quantitatively between the ground truth and model prediction, the MTRE and the MHRE were calculated for the test set and shown in Fig. 9.

The MTRE represented the accuracy of the surrogate model to the local information, while the MHRE represents the accuracy of the global information. The average MTRE of the whole test set is only 2.83% and the average MHRE is only 2.51% which shows that ASAP network model can not only accurately predict the maximum temperature in 50 test data but also produce details consistent with the actual image. As shown in Fig. 10, the average SSIM value of the temperature field image predicted by ASAP-net for the 50 cases in the test set reaches 0.945, proving that ASAP-net is capable of generating results similar to the ground truth.

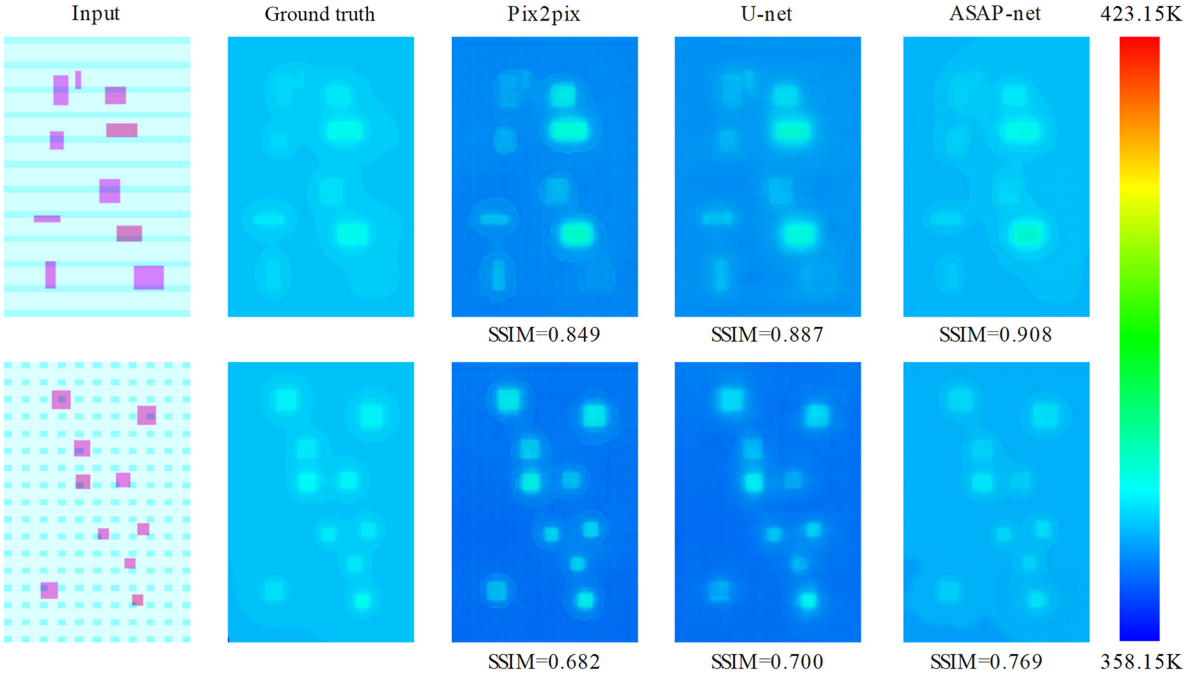

Fig. 6 Two cases selected from the test set, in which the outputs of Pix2pix model, U-net model, and ASAP-net were compared, respectively

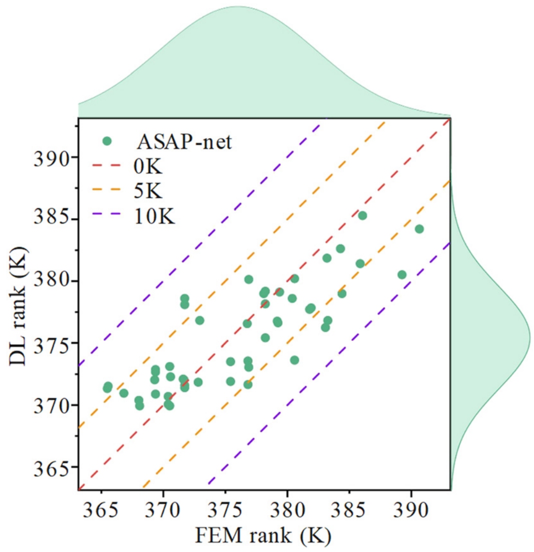

Fig. 8 Scatter plot of the maximum temperature values was obtained from the ground truth and DL model in the test set. The indication lines of 0 K, 5 K, and 10 K in the figure indicate the error interval corresponding to this point.

3.4 Performance Comparison of Different Scale of Training Set. The accuracy of the DL model is closely related to the amount of training data. To quantitatively describe the specific impact of the amount of data on the model performance, the training sets with different amounts of data, including 2, 4, 8, 16, 32, 64, and 128 cases, were randomly selected from natural convection dataset and used to train the ASAP-net model, respectively. The test set matched with each training set contained 50 cases. The model test results are shown in Fig. 11. It can be noted that when there is less data, the model can easily generate results that differ significantly from the actual temperature field distribution. And as the size of the training set keeps increasing, there were fewer and fewer discordant color blocks, and the image was closer to the ground truth.

To illustrate the difference of the maximum temperature error about models, the MTRE was studied in Fig. 12(*a*). When the model used only two cases, the test MTRE of the model ranged from 6.08% to 14.56%, and the interval length was 8.48%, which indicated the model was unstable and inaccurate. It was reasonable to suppose that too little training data could only guide the mapping relationship in a small part of the design space. When the amount of training data reached 128 cases, the MTRE was distributed in the interval of 2.45–5.73%, and the interval length was 3.28%. The MTRE distribution interval of repeated experiments became narrower and narrower, which indicated that the stability of the model would increase with the expansion of the training set. Meanwhile, it could be found that the downward trend of error in more than 32 cases had slowed down, which showed that the required amount of data could be greatly reduced by only sacrificing a small amount of model regression accuracy in some specific cases. It greatly reduced the difficulty of data collection and made practical engineering application possible.

As shown in Fig. 12(*b*), MHRE of the ASAP-net decreased with the expansion of the training set. Unlike MTRE, the MHRE represents the whole difference between the generated map and the ground truth, and the fidelity of the map generated by the model.

Due to the difficulty to map the field rich details, the downward trend of MHRE did not slow down under a certain amount of data, and more data were needed to increase the fitting ability. In addition, the SSIM of the model training results under different training set sizes is also calculated and compared (Fig. 13). It can be found that the structural similarity between the model output results, and the actual cloud image improves with the increase of training volume.

3.5 Performance Comparison of Fine-Tuning. In many practical projects, collecting a lot of data from a current problem to address is often time-consuming and impractical. A common model migration method is to pretrain a model on the collected datasets and then fine-tune the model with few data from the target project [35]. The weights trained with 170 natural convection cases were used as the pretrained weights of fine-tuning experiments. Sixteen air-cooling cases were used to train from scratch or fine-tune the pretrained model, and the test set was 50 air-cooling cases never seen in the training epochs. Compared with the model trained from scratch using the same 16 cases, the output of fine-tuning model was more realistic (Fig. 14). Similar conclusions can be found quantitatively in Figs. 15 and 16. The error of fine-tuning data model was smaller, and the whole image was closer to the ground truth. The output of the model trained from scratch showed unrealistic temperature distributions, which would lead to fatal errors in the calculation of temperature gradients at any position in the temperature field and in any direction.

By using the pretrained weights, the model had a 28.4% (Fig. 15(*a*)) and 25.4% (Fig. 15(*b*)) improvement in MTRE and MHRE, respectively. At the same time, the difference of the model performance under different datasets was smaller, and the reliability was higher. The reason is the weights of pretraining were closer to the global optimum than the weights of random initialization. The model only needed a small amount of data to modify and can predict the new distribution more accurately. The results achieved by fine-tuning were encouraging, which means that when we face a new problem, we can not only rely on the experience gained from the current problem but can also obtain guidance from historical data.

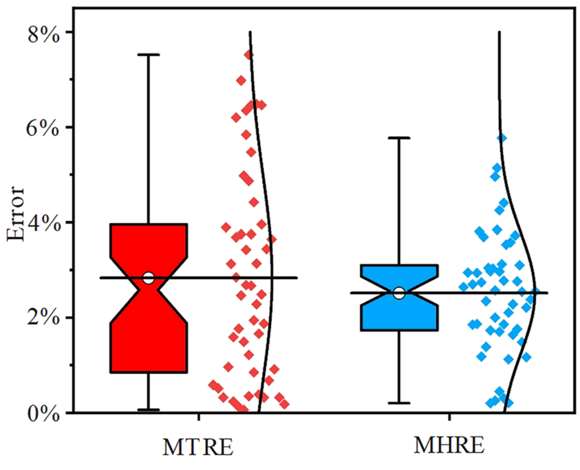

Fig. 9 Average MTRE and MHRE of ASAP-net in test set

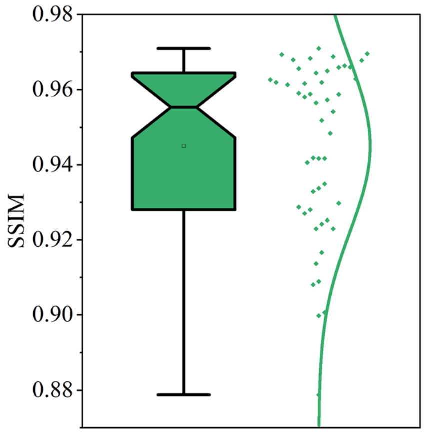

Fig. 10 SSIM values of ASAP-net's prediction results for the test set

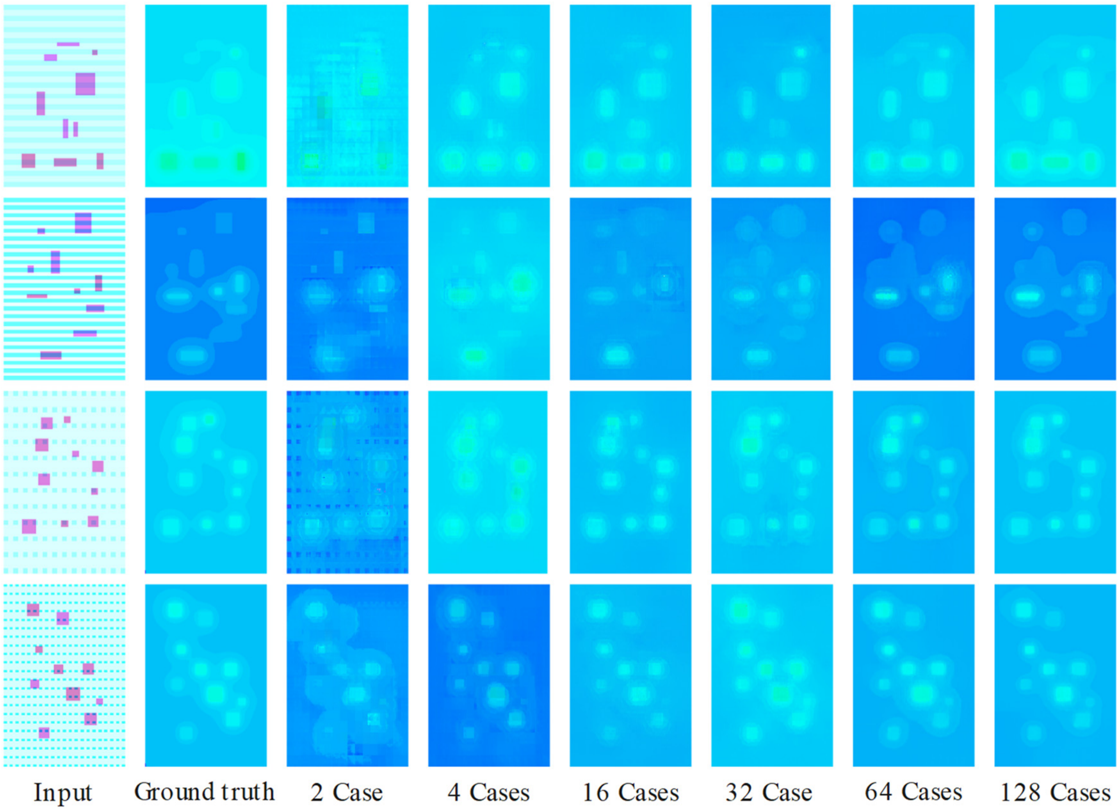

Fig. 11 Comparison of ASAP-net output temperature field trained using different sizes of training set

3.6 Time and Energy Consumption. Traditional CAE usually needs a lot of time and energy to solve thermal simulation problems [19]. As shown in Fig. 17, the time and energy consumption of ASAP-net test and training and CAE simulation cases were compared. Each mark in the figure represents the energy and time consumed by the corresponding program. It took an average time of 45.3 ms to calculate a temperature field using the ASAP-net model when testing 1000 geometry labels (Table 1). What's more, it only took an average time of 6.93 ms to predict a single temperature field after removing the time spent on model loading and image saving.

The time and energy consumed by model training were also measured. The time and energy consumed by training 500 epochs in the training sets of 1, 4, 16, and 32 cases are shown in Fig. 17. The time and energy consumed in training were linearly correlated in different size training sets. The energy consumed by NC (natural convection cases) and AC (air-cooling heat dissipation cases) was quite diverse because of the difference in geometry and initialization conditions of CAE. Additionally, given that ASAP-net demonstrated predictive capabilities with specific a MTRE of 2.83% and a MHRE of 2.51%, it warranted comparison against simulators

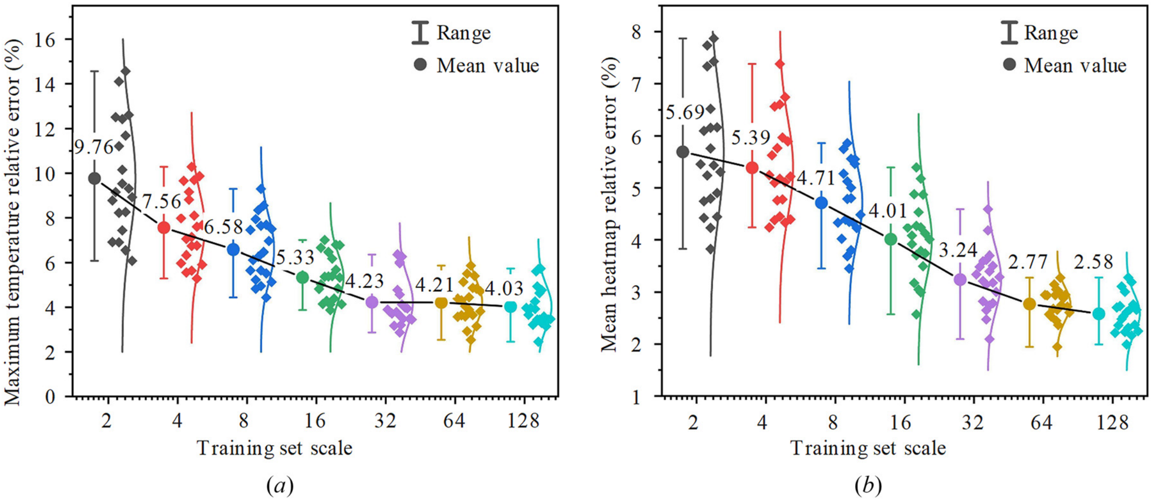

Fig. 12 Model performance comparison between different sizes of training set. (*a*) The influence of different sizes of training set on MTRE. Twenty sets of randomly sampled data were used to train the ASAP-net model from the sketch. (*b*) The influence of different sizes of training set on MHRE.

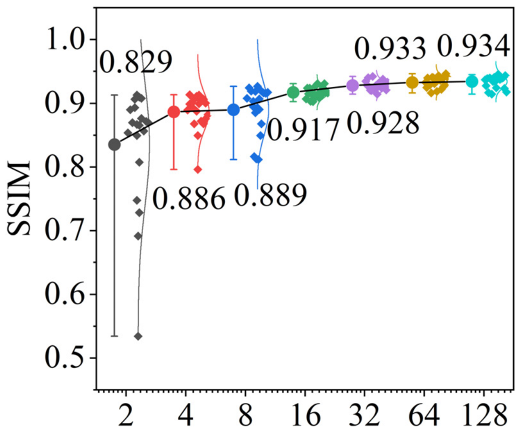

Fig. 13 SSIM values of prediction results obtained for different sizes of training set

employing coarser meshes and fewer iterations. As shown in Table S8 available in the Supplemental Materials on the ASME Digital Collection, simulations are conducted across varying mesh accuracies and iteration counts using a randomly selected parameter set. The outcomes from the most refined mesh and the longest iterations serve as the ground truth for assessing accuracy across different simulation settings. Comparative analysis reveals that ASAP-net's prediction process consumes 3 orders of magnitude less time and energy than simulators with similar error. For design optimization, it is very advantageous to calculate the steady-state temperature field of a geometric label in only several milliseconds, especially for algorithms that perform a large number of calculations and iteratively optimize the geometric design.

4 Discussion

In this work, cGAN method constructs a bridge between geometry and temperature field. When the amount of training data is small, the cGAN model can generate realistic but slightly less accurate images

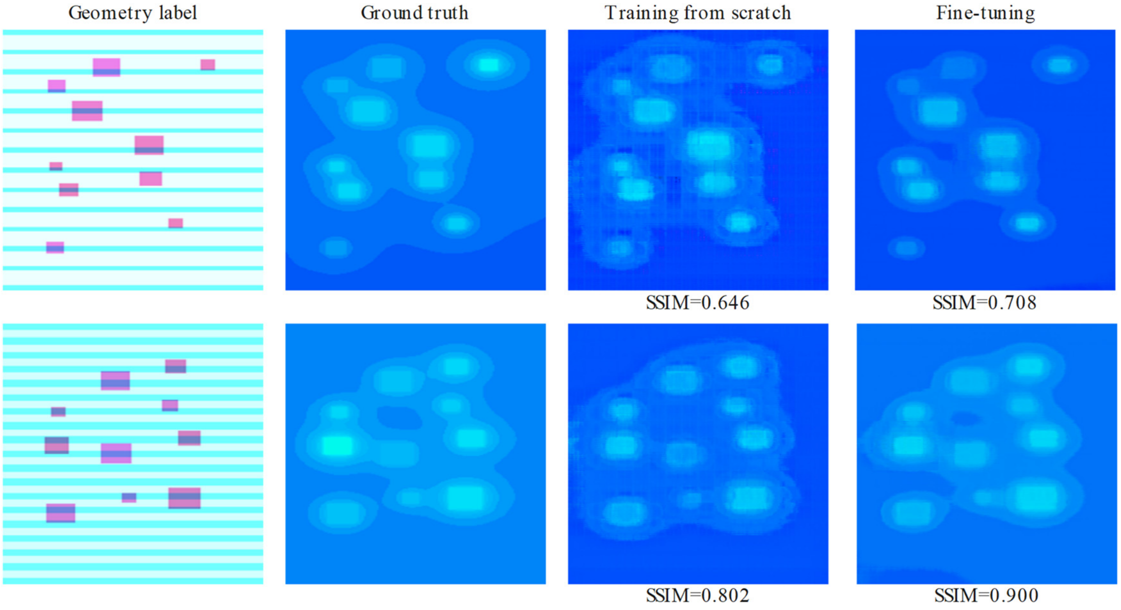

Fig. 14 Intuitive comparison of model output results corresponding to two geometries randomly selected from the first test sets

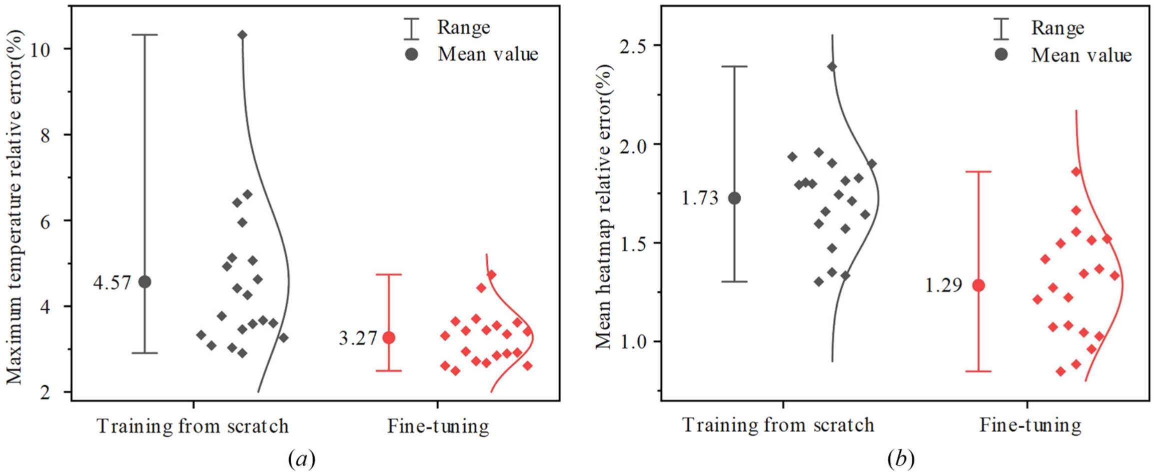

Fig. 15 Model performance comparisons of the fine-tuning results: (*a*) quantitative comparison of fine-tuning results with MTRE and (*b*) quantitative comparison of fine-tuning results with MHRE

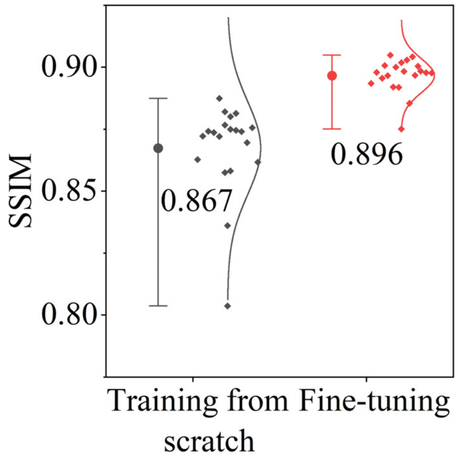

Fig. 16 Mean SSIM values for training from scratch versus fine-tuning

(Fig. 11). The results showed that the model achieved a satisfactory accuracy by fine-tuning the pretrained model (Fig. 14). This has laid a solid foundation for the cGAN methods to make an indelible contribution in the industrial field.

Due to the ingenious design of the geometry label, the method proposed by us was highly extensible for different geometric shapes. The geometry label of the model implemented in this paper was a picture with three channels represented the geometry of different modules from the actual thermal model. Similarly, by expanding the number of channels, we can achieve a more comprehensive generalization of the thermal model, including boundary conditions and special geometry. This means that with the expansion of label, the range of heat dissipation scenarios of electronic devices that can be accurately predicted gradually expands. In contrast to the expansion, we also provided performance exploration methods to narrow its application range. For the heat dissipation scenarios of electronic devices that were different from the limited conditions of precollected data, the model trained by using collected data cannot achieve a good performance. However, through the fine-tuning method, it only needs to collect several data of new scenarios to complete the model migration.

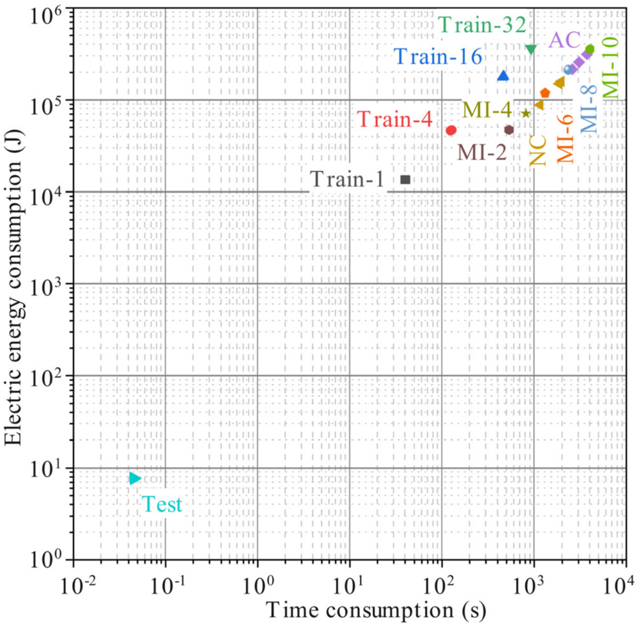

Fig. 17 Test represents the time and energy required to predict a temperature field. Train-*n* represents the time and energy consumed by using *n* data for 500 epochs of training, and NC and AC represent the time and energy consumed by the CAE programs of natural convection cooling and air-cooling heat dissipation to solve a case, respectively.

Compared with CAE simulation, the cGAN model has the unique advantages of very short prediction time and low energy consumption. The comparison of time and energy consumption is shown in Fig. 17. The power consumed by the computer for predicting a temperature field was only 2.93×10^{-5}–5.80×10^{-5} times that of a case calculated by CAE. By calling the trained ASAP-net, the program could obtain the corresponding steady-state temperature field at a speed of almost real-time response. The above advantages make the surrogate model constructed by cGAN methods applicable to the structural topology optimization dominated by swarm intelligence optimization methods [36–38] which needs a large number of calculation results, so as to find the optimal structure. Different from the number-to-number model on which the general topology optimization is based, the cGAN model of the complete field provided the two-dimensional topology optimization with more guidance information, which made the optimization more comprehensive. In addition, provided that the input signals possess adequate information content, the proposed method is applicable to a wide range of scenarios requiring the prediction of physical fields through structural relationships. Examples include the mapping relationships between airfoil structures and flow fields, and the rapid computation of force fields using the shapes of support components and constraints.

5 Conclusions

In this study, a strong mapping model from multistructure parameters to PCB steady-state temperature field distribution was established. In addition to comparing the established ASAP-net model with the other two baseline models, this paper also conducted experiments on the impact of different amounts of training data on the performance of the model and experiments on fine-tuning the model to adapt to the actual engineering conditions. Experiments indicated the following conclusions:

1. The ASAP-net model successfully reconstructed the temperature distribution on the PCB. Although the structure of fins and the distribution of heat sources were very diverse, and the temperature field had very rich contour details, the model could still better represent the mapping relationship between multi structure parameters and PCB temperature field.
2. In order to meet the requirements of small amount of data required by the actual use of the project, the amount of data and model accuracy were explored in the research, and it was found that when the amount of data was small, the requirements could be achieved by sacrificing part of the accuracy, which makes the actual use of the project possible.
3. In order to use historical data to solve new problems in engineering, the fine-tuning was studied, and it was found that with the increase of historical data, the new scene data required to achieve the same accuracy was gradually reduced, which was of great significance for practical engineering use.

This effort work took the advantage of deep learning approaches to model the 2D temperature distribution of PCB. Compared with the traditional one-dimensional methods, cGAN is a novel method, which can help researchers design the loss function of the model and generate the results approximating computational fluid dynamics data. In practical engineering, a rough model can be trained through a small amount of pre-experimental data or a more accurate model can be trained in combination with a prior database. It can provide a quick guidance for product thermal scheme design. However, there is no research on model adaptation except for electronic products instead of a fixed heat sink. For the current problem that the model outputs cloud maps with certain errors at low temperatures and far from the chip, it can be solved and studied in the future by adding physical information or using its rough model to fine-tune.

Specifically, by adding Dirichlet or Neumann boundary constraints to the loss function or discriminator to ensure that the model can output more accurate contour edges. Alternatively, a model with a small number of meshes or a highly simplified structure can be parametrically simulated enough times in an acceptable amount of time to collect enough data to pretrain the model. The model is then tuned to the situation and several accurate temperature maps are collected to fine-tune the pretrained model to achieve a sufficiently accurate model output. Continuous interaction, tracking, and efforts are essential in this cross-disciplinary region.

Funding Data

- National Key Research and Development Project (No. 2020YFB1711301; Funder ID: 10.13039/501100002855).
- National Natural Science Foundation of China (No. 51905178; Funder ID: 10.13039/501100001809).
- Natural Science Foundation of Guangdong Province, China (No. 2021B1515020087; Funder ID: 10.13039/501100003453).
- Fundamental Research Funds for the Central Universities, SCUT (Funder ID: 10.13039/501100012226).

Data Availability Statement

The datasets generated and supporting the findings of this article are obtainable from the corresponding author upon reasonable request.

Nomenclature

g = gravity, kg/m^3
h = enthalpy, J
h_w = convective heat transfer coefficient of the wall, W/(m^2 K)
H_{bump} = the height of the bump, mm
H_{sink} = the height of the fin, mm
k = molecular conductivity, W/(m K)
k_a = thermal conductivity of air, W/(m K)
k_w = thermal conductivity of the wall, W/(m K)
$\mathcal{L}_{\text{cGAN}}(G, D)$ = the loss function of the mean square error
$\mathcal{L}_1(G)$ = L1 loss function
MHRE = the mean heatmap relative error, %
MTRE = the maximum temperature relative error, %
P_{chips} = the thermal power of chips, W
SSIM = the structural similarity metric value
T = temperature of the fluid at specific location, K
T_a = temperature of air, K
T_{CAE} = maximum temperature of CAE simulation results, K
T_{DL} = the maximum temperature of DL predictions, K
T_w = temperature of the wall, K
T_0 = the ambient temperature, K
$\mathbf{v}$ = velocity vector of the fluid, m/s
β = thermal expansion coefficient, K^{-1}
∇T = gradient of temperature, K/m
λ = a super parameter used to weigh the relative importance of two errors
ρ = density of the fluid at specific location, kg/m^3
$\partial T/\partial n$ = gradient of temperature in the normal direction to the boundary, K/m

References

[1] Bell, L. E., 2008, "Cooling, Heating, Generating Power, and Recovering Waste Heat With Thermoelectric Systems," Science, **321**(5895), pp. 1457–1461.

[2] Farzanehnia, A., Khatibi, M., Sardarabadi, M., and Passandideh-Fard, M., 2019, "Experimental Investigation of Multiwall Carbon Nanotube/Paraffin Based Heat Sink for Electronic Device Thermal Management," Energy Convers. Manage., **179**, pp. 314–325.

[3] Moore, A. L., and Shi, L., 2014, "Emerging Challenges and Materials for Thermal Management of Electronics," Mater. Today, **17**(4), pp. 163–174.

[4] Wang, C., Hua, L., Yan, H., Li, B., Tu, Y., and Wang, R., 2020, "A Thermal Management Strategy for Electronic Devices Based on Moisture Sorption-Desorption Processes," Joule, **4**(2), pp. 435–447.

[5] Yadav, A. S., and Bhagoria, J. L., 2013, "Heat Transfer and Fluid Flow Analysis of Solar Air Heater: A Review of CFD Approach," Renewable Sustainable Energy Rev., **23**, pp. 60–79.

[6] Zhang, Q., Huo, Y., and Rao, Z., 2016, "Numerical Study on Solid–Liquid Phase Change in Paraffin as Phase Change Material for Battery Thermal Management," Sci. Bull., **61**(5), pp. 391–400.

[7] Mei, X., Xie, Y., Chai, S., Wu, X., and Lu, L., 2023, "Analysis of Liquid Film Evaporation in Porous Particles: Toward Optimal Wick Parameters for Heat Transfer in Heat Pipes," ASME J. Heat Mass Transfer-Trans. ASME, **145**(11), p. 111003.

[8] Dugast, F., Apostolou, P., Fernandez, A., Dong, W., Chen, Q., Strayer, S., Wicker, R., and To, A. C., 2021, "Part-Scale Thermal Process Modeling for Laser Powder Bed Fusion With Matrix-Free Method and GPU Computing," Addit. Manuf., **37**, p. 101732.

[9] Zandi, S., Seresht, M. J., Khan, A., and Gorji, N. E., 2022, "Simulation of Heat Loss in $\text{Cu}_2\text{ZnSn}_4\text{S}_x\text{Se}_{4\text{-x}}$ Thin Film Solar Cells: A Coupled Optical-Electrical-Thermal Modeling," Renewable Energy, **181**, pp. 320–328.

[10] Shojaei, A., 2003, "Simulation of the Three-Dimensional Non-Isothermal Mold Filling Process in Resin Transfer Molding," Compos. Sci. Technol., **63**(13), pp. 1931–1948.

[11] Shojaei, A., Ghaffarian, S. R., and Karimian, S. M. H., 2002, "Numerical Simulation of Three-Dimensional Mold Filling Process in Resin Transfer Molding Using Quasi-Steady State and Partial Saturation Formulations," Compos. Sci. Technol., **62**(6), pp. 861–879.

[12] Cho, S., Kim, M., Lyu, B., and Moon, I., 2021, "Optimization of an Explosive Waste Incinerator Via an Artificial Neural Network Surrogate Model," Chem. Eng. J., **407**, p. 126659.

[13] Wang, B., Xie, B., Xuan, J., and Jiao, K., 2020, "AI-Based Optimization of PEM Fuel Cell Catalyst Layers for Maximum Power Density Via Data-Driven Surrogate Modeling," Energy Convers. Manage., **205**, p. 112460.

[14] Navid, A., Khalilarya, S., and Taghavifar, H., 2016, "Comparing Multi-Objective Non-Evolutionary NLPQL and Evolutionary Genetic Algorithm Optimization of a DI Diesel Engine: DoE Estimation and Creating Surrogate Model," Energy Convers. Manage., **126**, pp. 385–399.

[15] Park, D., Cha, J., Kim, M., and Go, J. S., 2020, "Multi-Objective Optimization and Comparison of Surrogate Models for Separation Performances of Cyclone Separator Based on CFD, RSM, GMDH-Neural Network, Back Propagation-ANN and Genetic Algorithm," Eng. Appl. Comput. Fluid Mech., **14**(1), pp. 180–201.

[16] Li, H., Xu, B., Lu, G., Du, C., and Huang, N., 2021, "Multi-Objective Optimization of PEM Fuel Cell by Coupled Significant Variables Recognition, Surrogate Models and a Multi-Objective Genetic Algorithm," Energy Convers. Manage., **236**, p. 114063.

[17] Yang, Z., Yu, C.-H., and Buehler, M. J., 2021, "Deep Learning Model to Predict Complex Stress and Strain Fields in Hierarchical Composites," Sci. Adv., **7**(15), p. eabd7416.

[18] Yang, L., Wang, Q., and Rao, Y., 2021, "Searching for Irregular Pin-Fin Shapes for High Temperature Applications Using Deep Learning Methods," Int. J. Therm. Sci., **161**, p. 106746.

[19] Wang, Y., Zhou, J., Ren, Q., Li, Y., and Su, D., 2021, "3-D Steady Heat Conduction Solver Via Deep Learning," IEEE J. Multiscale Multiphys. Comput. Tech., **6**, pp. 100–108.

[20] Yang, Z., and Buehler, M. J., 2022, "Linking Atomic Structural Defects to Mesoscale Properties in Crystalline Solids Using Graph Neural Networks," npj Comput. Mater., **8**(1), p. 198.

[21] Chen, X., Chen, X., Zhou, W., Zhang, J., and Yao, W., 2020, "The Heat Source Layout Optimization Using Deep Learning Surrogate Modeling," Struct. Multidiscip. Optim., **62**(6), pp. 3127–3148.

[22] Zhao, X., Gong, Z., Zhang, J., Yao, W., and Chen, X., 2021, "A Surrogate Model With Data Augmentation and Deep Transfer Learning for Temperature Field Prediction of Heat Source Layout," Struct. Multidiscip. Optim., **64**(4), pp. 2287–2306.

[23] Chen, J., Zhu, F., Han, Y., and Chen, C., 2021, "Fast Prediction of Complicated Temperature Field Using Conditional Multi-Attention Generative Adversarial Networks (CMAGAN)," Expert Syst. Appl., **186**, p. 115727.

[24] Kang, M., Phuong Nguyen, N., and Kwon, B., 2024, "Deep Learning Model for Rapid Temperature Map Prediction in Transient Convection Process Using Conditional Generative Adversarial Networks," Therm. Sci. Eng. Prog., **49**, p. 102477.

[25] Edalatifar, M., Tavakoli, M. B., Ghalambaz, M., and Setoudeh, F., 2021, "Using Deep Learning to Learn Physics of Conduction Heat Transfer," J. Therm. Anal. Calorim., **146**(3), pp. 1435–1452.

[26] Paszke, A., Gross, S., Massa, F., Lerer, A., Bradbury, J., Chanan, G., Killeen, T., et al., 2019, "PyTorch: An Imperative Style, High-Performance Deep Learning Library," Adv. Neural Inf. Process. Syst., **32**, pp. 8026–8037.

[27] Shaham, T. R., Gharbi, M., Zhang, R., Shechtman, E., and Michaeli, T., 2021, "Spatially-Adaptive Pixelwise Networks for Fast Image Translation," IEEE/CVF Conference on Computer Vision and Pattern Recognition (CVPR), Nashville, TN, June 20–25, pp. 14877–14886.

[28] Isola, P., Zhu, J.-Y., Zhou, T., and Efros, A. A., 2017, "Image-to-Image Translation With Conditional Adversarial Networks," IEEE/CVF Conference on Computer Vision and Pattern Recognition (CVPR), Honolulu, HI, July 21–26, pp. 5967–5976.

[29] Ronneberger, O., Fischer, P., and Brox, T., 2015, "U-Net: Convolutional Networks for Biomedical Image Segmentation," *Medical Image Computing and Computer-Assisted Intervention—MICCAI 2015*: *18th International Conference,, Munich, Germany*, Oct. 5–9, pp. 234–241.

[30] Wang, Z., Bovik, A. C., Sheikh, H. R., and Simoncelli, E. P., 2004, "Image Quality Assessment: From Error Visibility to Structural Similarity," IEEE Trans. Image Process., **13**(4), pp. 600–612.

[31] Shields, M. D., and Zhang, J., 2016, "The Generalization of Latin Hypercube Sampling," Reliab. Eng. Syst. Saf., **148**, pp. 96–108.

[32] Ke, S., and Liu, W., 2022, "Consistency of Multiagent Distributed Generative Adversarial Networks," IEEE Trans. Cybern., **52**(6), pp. 4886–4896.

[33] Pakrouh, R., Hosseini, M. J., Ranjbar, A. A., and Bahrampoury, R., 2015, "A Numerical Method for PCM-Based Pin Fin Heat Sinks Optimization," Energy Convers. Manage., **103**, pp. 542–552.

[34] Nilpueng, K., Kaseethong, P., Mesgarpour, M., Shadloo, M. S., and Wongwises, S., 2022, "A Novel Temperature Prediction Method Without Using Energy Equation Based on Physics-Informed Neural Network (PINN): A Case Study on Plate-Circular/Square Pin-Fin Heat Sinks," Eng. Anal. Boundary Elem., **145**, pp. 404–417.

[35] Zhuang, F., Qi, Z., Duan, K., Xi, D., Zhu, Y., Zhu, H., Xiong, H., and He, Q., 2021, "A Comprehensive Survey on Transfer Learning," Proc. IEEE, **109**(1), pp. 43–76.

[36] Vučina, D., Marinić-Kragić, I., and Milas, Z., 2016, "Numerical Models for Robust Shape Optimization of Wind Turbine Blades," Renewable Energy, **87**, pp. 849–862.

[37] Hu, G., Li, M., Wang, X., Wei, G., and Chang, C.-T., 2022, "An Enhanced Manta Ray Foraging Optimization Algorithm for Shape Optimization of Complex CCG-Ball Curves," Knowl.-Based Syst., **240**, p. 108071.

[38] Rao, Y., He, D., and Qu, L., 2022, "A Probabilistic Simplified Sine Cosine Crow Search Algorithm for Global Optimization Problems," Eng. Comput., **39**(3), pp. 1823–1841.